COMMUNICATION

Multimodal Imaging of Autofluorescent Sites Reveals Varied Chemical Speciation in SSZ-13 Crystals

Naomi Omori*[a, +], Alessia Candeo*[b, +], Sara Mosca[b], Ines Lezcano-Gonzalez[a], Ian K. Robinson[c], Luxi Li[d], Alex G. Greenaway[a], Paul Collier[e], and Andrew M. Beale*[a]

[a] N. Omori [+], I Lezcano-Gonzalez, A. G. Greenaway, A. M. Beale
Department of Chemistry
University College London
20 Gordon Street, London, WC1H 0AJ, UK
E-mail: neomori@gmail.com
and
The Research Complex at Harwell, Rutherford Appleton Laboratory
Harwell Campus, Didcot, Oxfordshire, OX11 0FA, UK
E-mail: Andrew.beale@ucl.ac.uk

[b] A Candeo [+], S Mosca
Central Laser Facility—Science & Technology Facility Council
The Research Complex at Harwell, Rutherford Appleton Laboratory
Harwell Campus, Didcot, Oxfordshire, OX11 0FA, UK
Email: alessia.candeo@stfc.ac.uk

[c] I. K. Robinson
London Centre for Nanotechnology
University College London
WC1E 6BT
and
Brookhaven National Laboratory
Upton, NY

[d] L. Li
Advanced Photon Source
Argonne National Laboratory
9700 South Cass Avenue
Lemont, IL 60439, USA9

[e] P. Collier
Johnson Matthey Technology Centre
Blounts Court Road, Sonning Common
Reading RG4 9NH, UK

Supporting information for this article is given via a link at the end of the document

[+] These authors contributed equally to this work

Abstract: *A multimodal imaging study of chabazite is used to show the distribution of and discriminate between different emissive deposits arising as a result of the detemplation process. Confocal imaging, 3D fluorescence lifetime imaging, 3D multispectral fluorescence imaging, and Raman mapping are used to show three different types of emissive behaviours each characterised by different spatial distributions, trends in lifetime, spectral signals, and Raman signatures. A notable difference is seen in the morphology of agglomerated surface deposits and larger subsurface deposits, which experience lifetime augmentation due to spatial confinement. The distribution of organic residue throughout the crystal volume is comparable to XRF mapping that shows Si enrichment on the outer edges and higher Al content through the centre, demonstrating that a fluorescence-based technique can also be used to indirectly comment on the compositional chemistry of the inorganic framework.*

Zeolites are an important class of materials that are well established as heterogeneous catalysts in the petrochemical industry[1], ion-exchange applications, and automotive emissions control[2]. In all these fields, there exists an ongoing need to improve zeolite performance from both an economics and sustainability perspective. In designing optimised zeolitic catalysts, a detailed understanding of the relationship between their structure and function is generally required, which has in turn led to an increased experimental emphasis on imaging techniques.

The primary challenge of imaging zeolites lies in their structurally and chemically complex internal landscapes, which are a unique combination of inorganic and organic material components. The inorganic aluminosilicate framework, which may be ion-exchanged with metals, dominates as a percentage mass and dictates the broader structure of the system, while the concomitant adsorbed organic phase that occupies the framework's internal free volume represents both the intended primary catalytic products (e.g. reactive intermediates) and secondary reaction by-products (e.g. coking).

It is extremely difficult to holistically visualise both the inorganic framework and the organic product phase in a single micrographic frame due to their vastly disparate requirements for generating image contrast. While the framework can be resolved with mainstay high resolution imaging modalities such as scanning electron microscopy (SEM)[3], transmission electron microscopy (TEM)[4], scanning tunnelling microscopy (STEM), or even tomography techniques[5], organic components are not readily resolved with these methods due to their light molecular mass. One option for visualising organic products in zeolites that has gained modest traction in the past decade is optical fluorescence imaging[6,7]. Incidentally, the majority of these studies probe the hierarchical structure of the framework and indicate the location of active sites by introducing and imaging a fluorescent [8–17], while comparatively sparse[18], have the distinct advantage of being able to directly comment on the chemistry of emissive organic products that build-up during processes like detemplation or catalytic fast pyrolysis of biomass, where coke has been shown to form

preferentially on Brønsted sites[19]. Karwacki *et al.* monitored the distribution and intensity of fluorescence emission across micrometre sized ZSM-5[20],[21], SAPO-34[20], SAPO-5[20], and CrAPO-5[20] crystals during detemplation, which is the final step in template-stabilised zeolite synthesis that aims to render the zeolite catalytically active by evacuating organic structure directing agent (OSDA) from the internal pore volume and is typically achieved by heating the material to around 550 °C. Specifically, by combining *in situ* confocal imaging and UV-Vis spectroscopy Karwacki *et al.* were able to monitor the formation of light absorbing and emitting species during the detemplation process, showing that the accessibility of the porous network varied depending on the framework family[20]. This study is of primary interest because it demonstrates how laser-based microscopy is capable of throwing sharp relief on the elusive yet chemically interesting organic phase, illuminating its distribution against the framework in a manner hitherto unachieved by electron imaging techniques.

This paper demonstrates how the combination of confocal imaging, 3D fluorescence lifetime imaging (FLIM) and 3D multispectral fluorescence imaging alongside Raman and XRF mapping provides enhanced insight into the distribution of template-derived organic products. The study focuses on the detemplation of a model 30 µm chabazite sample set whose photoluminescence dynamics during detemplation have been previously studied under UV spectroscopic conditions[22]. These crystallites are ideal candidates for micro-spectroscopic interrogation since they are large enough to visualise compositional variation but small enough to remain catalytically relevant, being only an order of magnitude greater in size than the crystallites used in real industry. Two samples were studied, one calcined at 550 °C and the other at 630 °C in an attempt to compare how the low levels of residual carbon-containing species evolve with temperature. The sample preparation is described in Section 1.1 in the Supporting Information. Standard SEM, TGA, and XRD characterisations were carried out and the methods can be found in Sections 1.2-1.4 in the Supporting Information, while the results are reported in Section 2.1-2.3 in the Supporting Information. However, none of these techniques can present a spatially resolved study of the products present in the crystals.

Instead, fluorescence microscopy is a powerful tool for the three-dimensional visualization of the fluorescent species present in single crystals. To ensure that the OSDA is not the species emitting primarily at the excitation wavelengths spectrofluorometer experiments were conducted (see Supporting Information, Section 2.4).

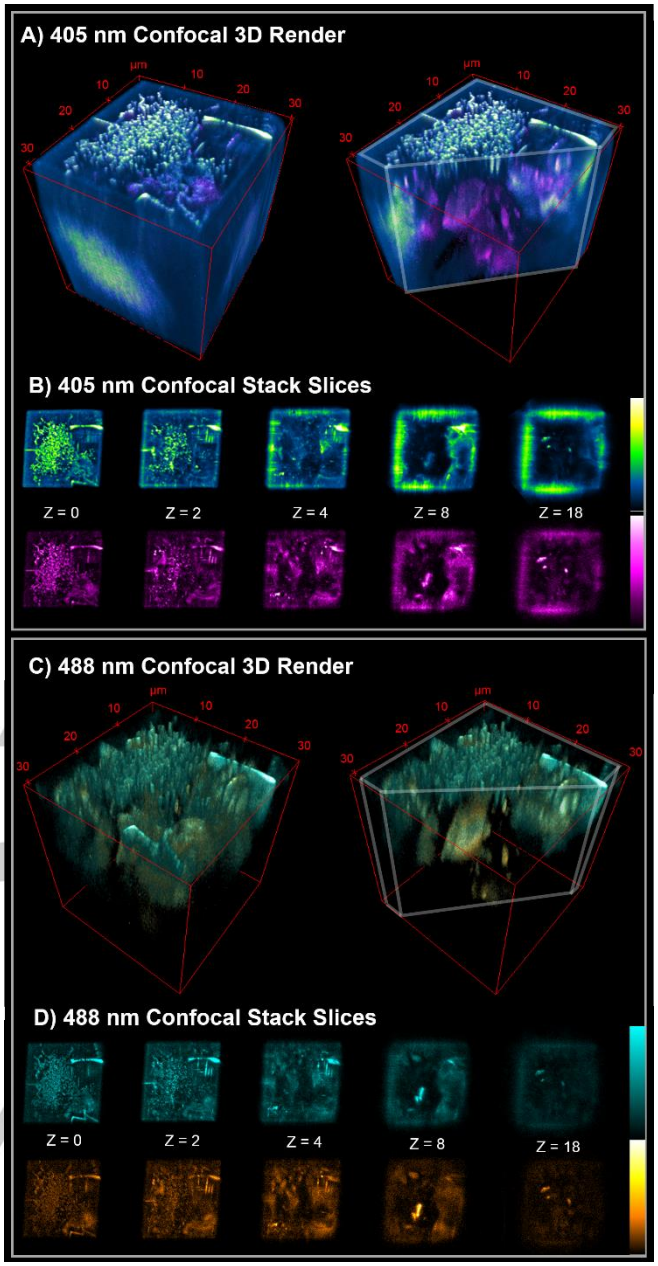

Figure 1. 3D image z-stack reconstruction of chabazite calcined at 550 °C: A) 3D rendering of the two-colour confocal laser microscopy z-stack (number of steps = 160; step interval 0.24 µm) acquired at λ_{ex}=405 nm where the blue-green channel captures emission from 450-550 nm and the magenta channel from 580-700 nm. B) Selected slices at various depths expressed in µm of the two separate channels of the 3D stack in A. C) 3D rendering of the two-colour confocal laser microscopy z-stack (number of steps = 160; step interval 0.24 µm) acquired at λ_{ex}=488 nm where the cyan channel captures emission from 500-550 nm and the orange channel from 580-700 nm. D) Selected slices at various depths expressed in µm of the two separate channels of the 3D stack in C.

Figure 1 shows 3D reconstructions generated from a series of fluorescence micrographs (Figure 1B, D, Supplementary Figure S6) acquired with two separate detection channels for a cubic chabazite crystal calcined at 550 °C excited at 405 nm (Figure 1A, detection channels 450-550 nm and 580-650 nm) and 488 nm (Figure 1C, detection channels 500-550 nm and 580-700 nm) with a confocal microscope (Supporting Information, Section 1.5 and Figure S5). The excitation wavelength 405 nm was the lowest and most efficient wavelength available for confocal imaging, and 488 nm was the lowest available pulsed wavelength for FLIM. A complex distribution of emissive products can be seen. Localised within

3 µm of the crystal surface and clustered towards the centre is a constellation of small agglomerates that are most strongly emissive in the bluer range. Towards the centre of the crystal volume is another type of deposit distributed across a range of depths featuring stronger, red-shifted fluorescence. Morphologically, they don't immediately appear to be governed by pore structure or crystallographic geometric restrictions.

The fluorescence emission observed in confocal imaging can be further analysed in terms of its lifetime, τ, and its spectrum. The lifetime of a fluorophore is a function of both the molecule itself and its interactions with its immediate environment. This makes it possible to speculate on chemical behaviours and interactions within the zeolite. Therefore, FLIM[23] was used to generate a spatial representation of the lifetimes of the present species (see Supporting Information, Section 1.6) by attributing the decay information of a specific point to the respective pixel in the image. FLIM has been performed in tagged [24,25] and metal-organic frameworks (MOFs)[26] but not on the natively occurring organic product hosted in the pores. Used in autofluorescent samples, FLIM enhances the information gained from conventional confocal microscopy allowing one to comment more extensively on speciation.

Figure 2 shows FLIM images obtained at 488 nm excitation of two planes of the same chabazite crystal: an external face (A1), and an inner plane 12 µm below the external plane (A2). The colour-scale is representative of the weighted mean lifetime of fluorescence emission, where red corresponds to longer lifetimes and blue to shorter ones. To quantify the differences in lifetime, the phasor method[27] was first used to qualitatively select regions of interest (ROI). Figure 2B1 and 2B2 show the phasor plots of the surface and inner planes, respectively. In the phasor plot, pixels characterised by shorter lifetimes generate peaks at small angles to the universal circle, while longer ones create peaks at larger angles. Phasor peaks closer to the universal circle can be described with a lower number of decay components, while peaks closer to the centre speak to a more complex behaviour. Figure 2B2 shows the presence of a larger variety of lifetimes both in the shorter and the longer timescales for the inner plane compared to the upper plane in Figure 2B1, which is also confirmed by the lifetime histograms in Figure 2D1 and 2D2.

Lifetime decays for each ROI are presented in Figure 2C and a summary of the extracted lifetimes values is presented in Supporting Information, Section 2.5, Table S1. On the upper plane ROI 1 highlights the surface agglomerates, which are also captured for a perpendicular plane in ROI 2 of the inner plane. Extracted values in Table S1 show that in the upper plane, ROI 1 and ROI 2 have different decay dynamics, with the first being biexponential, and the second being triexponential. However, ROI 1 from the top and ROI 2 from the inner plane have a comparable biexponential decay. The inner plane also shows clusters of material with a faster decay, as well as shorter ones, highlighting the complexity of the crystal core. By performing the acquisition of a stack of FLIM images, a 3D FLIM rendering can be made. In the 3D FLIM reconstruction in Figure 2F, we can observe that the faces of the crystal are all similar, with a difference between the central and the outer surface. Moreover, we can see how heterogenous the distribution of emissive products inside the crystal is. The crystal has been further analysed with multispectral fluorescence imaging[28–30], a technique where each pixel in the image contains the spectral information of the specific fluorophores present in that location (see Supporting Information, Section 1.7). The average spectra extracted from each ROI are presented in Figure 2E at both the 405 nm and 448 nm excitation. Interestingly, the emission spectra of ROI 1 and 2 of the surface of the crystal are the same. Moreover, the inner compounds show a broader and red-shifted spectrum compared to the surface, with some differences between clusters of materials.

At this point, the following chemical statements can be made. Based on the wavelength of excitation (i.e. 405 and 488 nm for confocal, 488 nm for FLIM), there are only a limited number of molecular species that will be emissive. These are polycyclic aromatic hydrocarbons[31,32] (PAH) and carbon nanostructures[33–36]. It has previously been demonstrated that the original quaternary ammonium templating material is not sufficiently excited with a visible source[22] and that the zeolite framework itself is optically transparent at this wavelength because the energy of excitation is too low. Therefore, it is expected that the emissive deposits being imaged are species that have formed through sequential OSDA decomposition, involving fragmentation and the subsequent formation of polyaromatics via cracking or aromatisation followed by ring condensation[37].

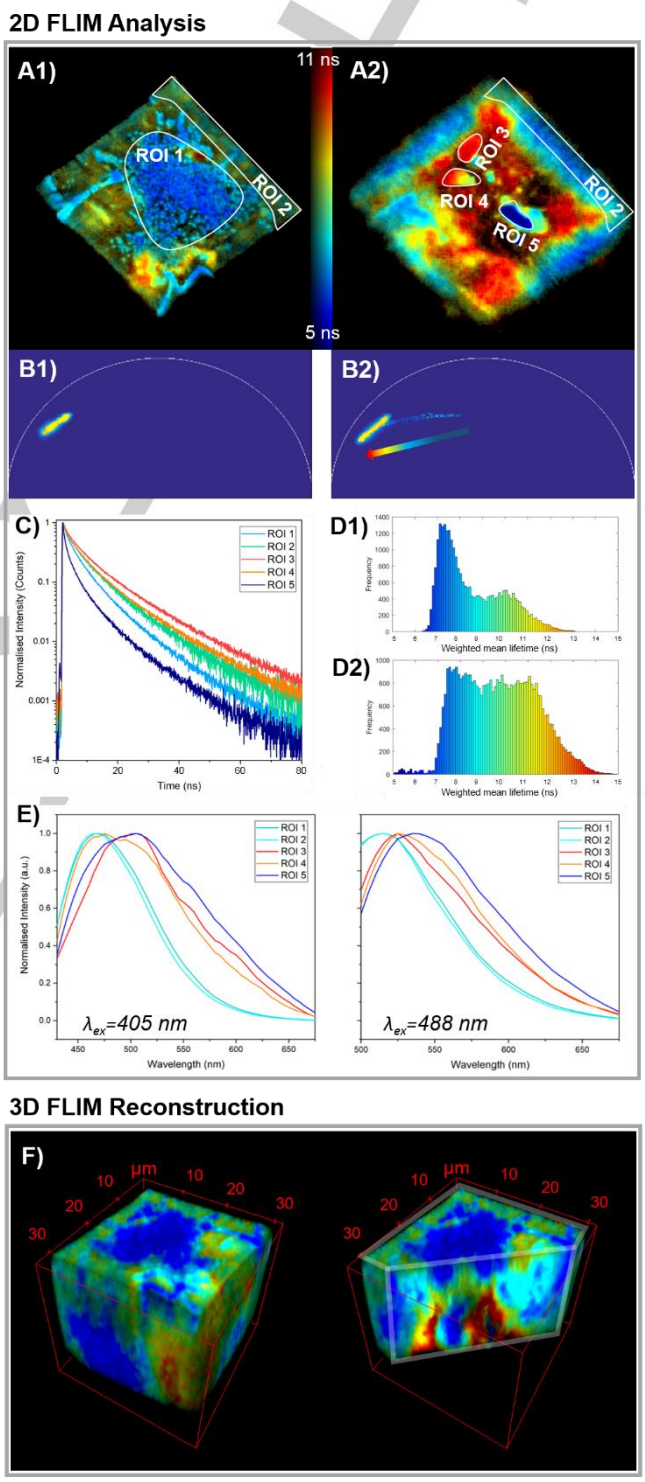

Figure 2. Single-channel fluorescence lifetime imaging ensemble of chabazite calcined at 550 °C acquired at λ_{ex}= 488 nm including the map of weighted average lifetimes A1) for the uppermost plane and A2) for the central plane and the respective phasor plots B1) and B2), C) the fluorescence decays for the selected ROIs indicated in A1) and A2), the respective frequency histograms of lifetimes D1) and D2), and E) the spectra for corresponding ROIs

acquired at λ_{ex}= 405 nm and 488 nm. F) 3D reconstruction of the FLIM stack (depth of only 25 µm)

Given that ROI 1 and 2 on the crystal surface have the same spectrum but different lifetimes, it can be inferred that the emissive species are similar, but that the local environment is influencing the decay. It would seem that the emissive products in the centre of the surface plane are less dispersed and less confined compared to the edges of the crystal. The larger red regions in the central FLIM plane indicating average lifetimes in excess of 10 ns can be attributed to the greater degree of confinement emissive materials will experience this deep within the crystal. Steric confinement of guest species has previously been shown to induce longer lifetimes in fluorophores as well as red-shifted emission as a result of the reduction in self-quenching associated with molecular twisting and [22,38,39]. These deposits appear to be clustered in the very centre of the crystal, and tend not to impinge upon the outer edges, creating what could be perceived as a 'zoning effect'. This effect can also be seen in the 3D reconstructions presented in Figure 1. Particular attention is drawn to ROI 5, which not only exhibits a shorter average lifetime, but also has a strong multi-exponential behaviour, as evidenced by the trailing tail in the phasor plot. It also features a broader spectral peak at 515 nm rather than 465 nm at λ_{ex}=405 nm, and a peak red-shifted by about 25 nm at λ_{ex}=488 nm, indicating that this emissive species is likely to be chemically distinct. It is perhaps the case that these regions represent areas where new hydrocarbon chemistry secondary to the combustion of the OSDA may have begun to take place[40].

Highlighting the technique's sensitivity to sample differences, 3D stacks of a chabazite crystal calcined at 630 °C were acquired and the 2-colours 3D rendering together with a selection of the single planes are presented in Figure S7 and S8. Figure 3 shows FLIM data from the uppermost plane and an inner plane of the very same crystal calcined at 630 °C. Overall, the emission intensity of this crystal is lower, which primarily relates to the lower concentration of organic material but also relates to the difference in products present. 3D FLIM reconstruction in Figure 3F shows the presence of a few highly fluorescent surface deposits and some clusters of material in the core but generally a lower degree of absorption and emission through the bulk of the crystal. Overall, the majority of short-living deposits are localised on crystal surface, while in the centre the lifetimes of the compounds are more long-living, correlating to the lengthening of lifetimes seen due to spatial confinement (see Supporting Information, Section 2.5, Table S2). Comparing the phasor plots and the lifetime histogram of this sample calcined at 630 °C to the first one calcined at 550 °C, it also appears that there is a broader variety of lifetimes and the spectra in Figure 3E are broader towards the red region of the spectrum. This is again compatible with a higher confinement of the fluorescent products. While there is some morphological commonality between subsurface deposits in Figure 2 and Figure 3, the fine distribution of surface deposits in the sample calcined at 550 °C are absent in this sample, with the majority of the decays being tri-exponential and no spectra matching to ROI 1 or 2 in Figure 2.

Based on morphology, lifetime, and spectra there appear to be at least three distinct types of emissive deposits (Figure S9). The first are the well-defined agglomerates clustered on the surface that are roughly 400 nm in diameter, which feature a weighted average lifetime of around 4 ns. appearing to originate from the centre of the crystal in the partially detemplated sample and emanating towards the surface of the crystal in the sample calcined at 550 °C, possibly comprised of late products like substituted PAHs (likely arising from OSDA fragmentation, followed by cracking/aromatisation and subsequent ring condensation). The second and third types of emissive deposits are the larger subsurface regions, one of which is smaller, features a faster average lifetime of around 2 ns, and has a peak emission at 495 nm and could be assigned to a combination of PAHs and carbon nanodots, which have been shown to form readily in zeolites under conventional thermal heating conditions[33]. The other type are larger subsurface deposits, with a longer average weighted lifetime of around 6 ns and an emission peak at 465 nm. These are identified as late products of hydrocarbon chemistry that are being influenced by the confinement effects of the framework. It is expected that greater steric confinement from being located deeper within the crystal is likely to yield longer lifetimes[38].

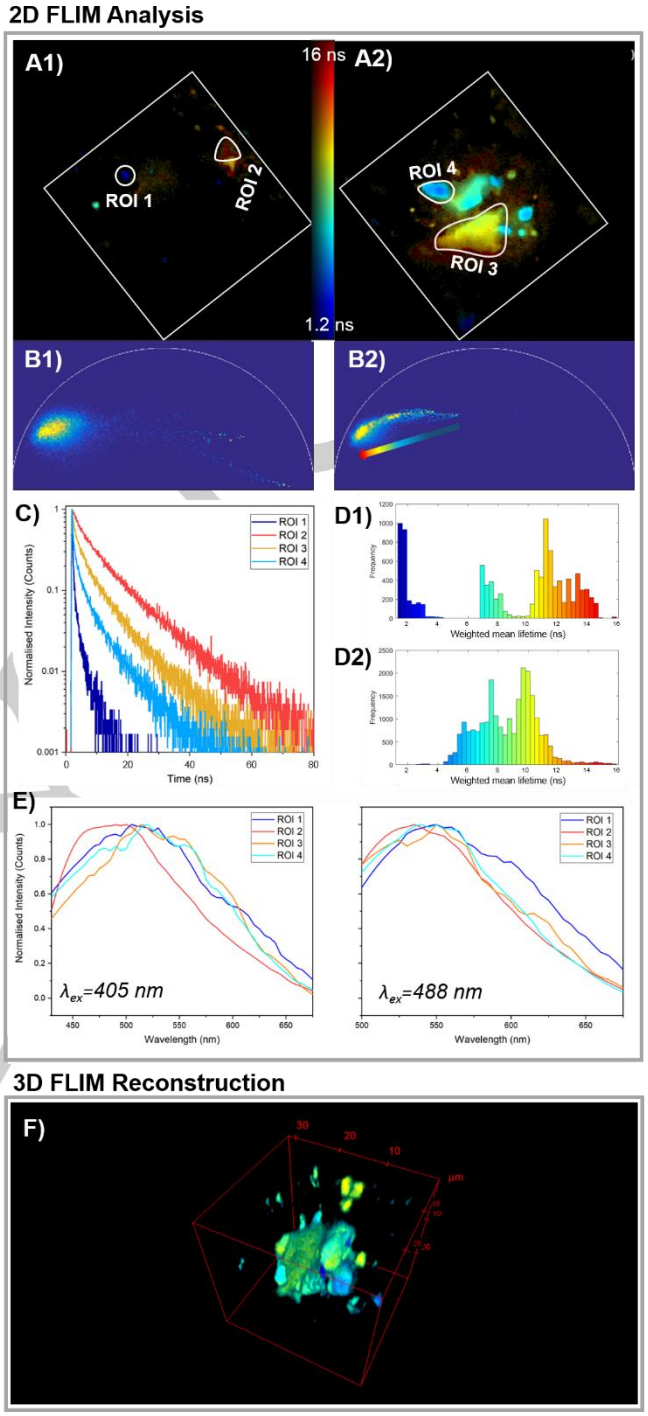

Figure 3. Single-channel fluorescence lifetime imaging ensemble of chabazite calcined at 630 °C acquired at λ_{ex}= 488 nm including the map of weighted average lifetimes A1) for the uppermost plane and A2) for the central plane and the respective phasor plots B1) and B2), C) the fluorescence decays for the selected ROIs indicated in A1) and A2), the respective frequency histograms of lifetimes D1) and D2), and E) the spectra for corresponding ROIs acquired at λ_{ex}= 405 and 488 nm. F) 3D reconstruction of the FLIM stack.

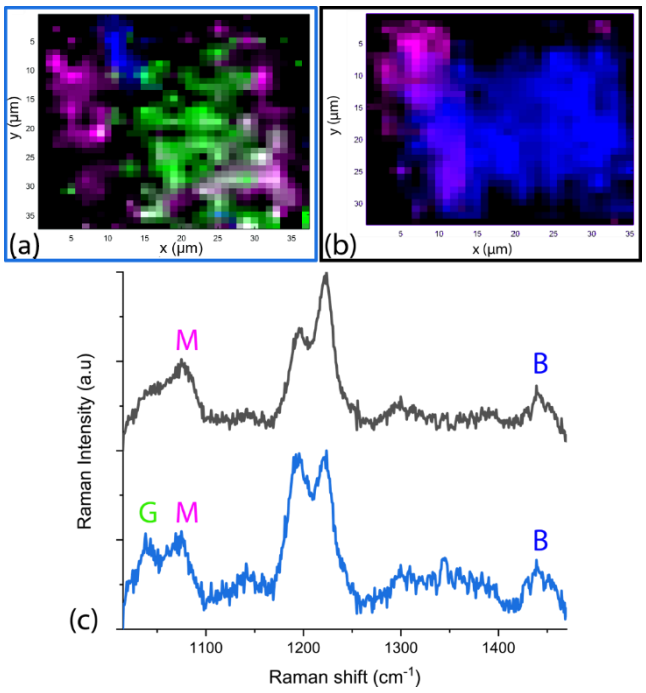

Figure 4. Raman maps showing the distribution of selected vibrations for A) chabazite calcined at 550 °C, B) chabazite calcined at 630 °C, and C) the average Raman spectra for the whole crystals are displayed (bottom blue one calcined at 550 °C, top black one calcined at 630 °C).

As a comparator, established techniques like Raman mapping and X-ray fluorescence tomography are utilised. Figure 4 shows Raman maps of crystal from the same batch of samples (see Supporting Information, Section 1.8). The region between 1015-1470 cm^{-1} was selected with the view to detect residual template derivatives. There are visible bands at 1038, 1075, 1195, 1223, and 1439 cm^{-1}. The doublet at 1195 and 1223 cm^{-1} is assigned to asymmetric T-O framework stretches[41,42]. The remaining bands are assigned to organic species. PAHs have been previously shown to exhibit bands in this region[43,44]. Figure 4A shows a varied distribution of Raman peaks, with 1038 cm^{-1} distributed across the centre in a manner similar to the agglomerated deposits of Figure 2A1, and 1075 and 1439 cm^{-1} concentrated in deposits in a similar manner to the subsurface regions visible in the inner plane in Figure 2A2.

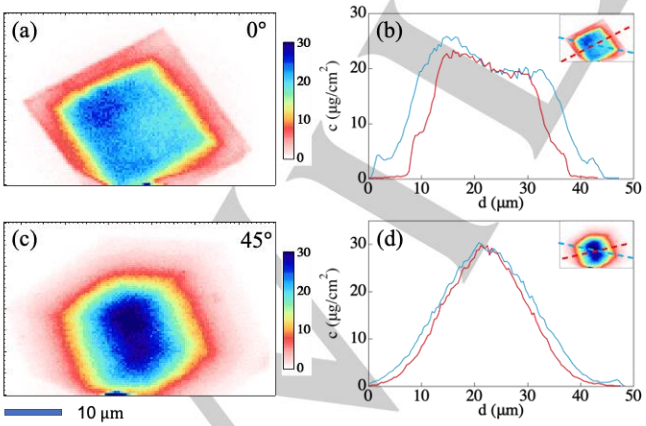

Figure 5. XRF tomography of wet-ion exchanged Cu-SSZ-13 crystals obtained at the 2-ID-E microprobe hard X-ray beamline at the Advanced Photon Source of Argonne National Laboratory with 10 keV photons. (a) and (c) are the projected Cu maps at 0º and 45º to the crystal block. (b) and (d) show line profiles from (a) and (c), respectively. Si and Al fluorescent signals were so low in energy they showed serious self-absorption effects and are not presented here.

XRF is a technique already used to analyse composition and elemental distributions in zeolite samples (see Supporting Information, Section 1.9). In Cu-SSZ-13, XRF slices for Cu presented in Figure 5 without self-absorption correction show a characteristic Cu zoning effect with a uniform distribution on the inside of the crystal and a suppressed signal along the outermost 7-8 μm of crystal edges (Figure 5A). The line-scan of the projection in Figure 5B shows a roughly linear Cu concentration profile ending at a sharp internal boundary, indicating a uniform distribution of Cu through the central 15 μm of the crystal, but linearly tapered over the outer 7-8 μm. Given its cubic morphology, this is not due to the shape in this projection looking along the crystal edges. The 45º view of the block in Figure 5C & D has a more graded appearance, which could be due to copper being washed out of the outer regions. It is interesting to note that the spatial distributions of emissive species in Figure 1 seem to correlate similarly with a concentration of Cu towards the centre of the crystal. Given that the Cu-exchange sites are associated with the distribution of Al, it follows also that template derivatives would also be able to mirror this effective Al distribution as the OSDA cations will also be preferentially located around the charge-introducing Al sites[45]. As such, on the basis of their chemical relationship to the framework, the emissive deposits are in fact able to indirectly provide information on the distribution of framework elements as well as the distribution of the organic phase themselves, providing even further insight than what XRF mapping is already providing.

FLIM maps, then, are not necessarily of interest because the numerical lifetime values are independently meaningful, but rather because they become useful if they are viewed as a map representative of degrees of confinement and chemical influence from factors like Si/Al concentration. Beyond simply showing distributions of hydrocarbons where lifetimes correlate to chemical species, FLIM also reveals variability in the crystal's local chemical environment by showing the degree to which it influences the lifetime of a guest species. In this sense, FLIM & confocal images provide a wholly unique way of visualising a zeolite and represent perhaps the closest iteration of a chemist's ideal imaging modality as they elucidate the arguably intangible concept of a 'chemical environment'. Systematic experimentation imaging families of zeolites synthesised and reacted under strict conditions will likely yield abundantly useful datasets that provide insight into how the chemical environment changes and influences catalysis. Additionally, the techniques can be extended into other inorganic materials as well as incorporated with *in situ* and *operando* setups to provide enhanced temporal resolution.

Acknowledgements

We should thank JM & EPSRC for funding a case award for Naomi Omori – voucher number 15220110. We also thank the EPSRC sponsored UK Catalysis Hub for funding the project of A. G. Greenaway (EP/K014714/1). Work at Brookhaven National Laboratory was supported by the U.S. Department of Energy, Office of Science, Office of Basic Energy Sciences, under Contract No. DE-SC0012704.
The Advanced Photon Source is supported by the US Department of Energy, Office of Science, Office of Basic Energy Sciences, under Contract No. DE-AC02-06CH11357.

Keywords: Zeolite • Imaging • Multimodal • Raman • Fluorescence

References

[1] E. T. C. Vogt, B. M. Weckhuysen, *Chem. Soc. Rev.* **2015**, *44*, 7342–7370.
[2] S. Brandenberger, O. Kröcher, A. Tissler, R. Althoff, *The State of the Art in Selective Catalytic Reduction of NOx by Ammonia Using Metal-Exchanged Zeolite Catalysts*, **2008**.
[3] K. Jansen, in (Eds.: H. Robson, K.P.B.T.-V.S. of Z.M. Lillerud), Elsevier Science, Amsterdam, **2001**, pp. 55–56.
[4] W. Wan, J. Su, X. D. Zou, T. Willhammar, *Inorg. Chem. Front.* **2018**, *5*, 2836–2855.
[5] J. E. Schmidt, R. Oord, W. Guo, J. D. Poplawsky, B. M. Weckhuysen, *Nat. Commun.* **2017**, *8*, 1–8.
[6] M. B. J. Roeffaers, J. Hofkens, G. De Cremer, F. C. De Schryver, P. A. Jacobs, D. E. De Vos, B. F. Sels, *Catal. Today* **2007**, *126*, 44–53.
[7] J. Van Loon, A. V. Kubarev, M. B. J. Roeffaers, *ChemNanoMat* **2018**, *4*, 6–14.
[8] G. Bonilla, M. Tsapatsis, D. G. Vlachos, G. Xomeritakis, *J. Memb. Sci.* **2001**, *182*, 103–109.
[9] I. L. C. Buurmans, J. Ruiz-Martínez, W. V. Knowles, D. Van Der Beek, J. A. Bergwerff, E. T. C. Vogt, B. M. Weckhuysen, *Nat. Chem.* **2011**, *3*, 862–867.
[10] G. T. Whiting, F. Meirer, D. Valencia, M. M. Mertens, A. J. Bons, B. M. Weiss, P. A. Stevens, E. de Smit, B. M. Weckhuysen, *Phys. Chem. Chem. Phys.* **2014**, *16*, 21531–21542.
[11] Z. Ristanović, J. P. Hofmann, G. De Cremer, A. V. Kubarev, M. Rohnke, F. Meirer, J. Hofkens, M. B. J. Roeffaers, B. M. Weckhuysen, *J. Am. Chem. Soc.* **2015**, *137*, 6559–6568.
[12] G. De Cremer, B. Sels, D. De Vos, J. Hofkens, M. Roeffaers, **2011**, pp. 245–261.
[13] Z. Ristanović, M. M. Kerssens, A. V. Kubarev, F. C. Hendriks, P. Dedecker, J. Hofkens, M. B. J. Roeffaers, B. M. Weckhuysen, *Angew. Chemie - Int. Ed.* **2015**, *54*, 1836–1840.
[14] A. Layek, J. Van Loon, M. B. J. Roeffaers, A. V. Kubarev, *Catal. Sci. Technol.* **2019**, *9*, 4645–4650.
[15] J. Van Loon, K. P. F. Janssen, T. Franklin, A. V. Kubarev, J. A. Steele, E. Debroye, E. Breynaert, J. A. Martens, M. B. J. Roeffaers, *ACS Catal.* **2017**, *7*, 5234–5242.
[16] F. C. Hendriks, S. Mohammadian, Z. Ristanović, S. Kalirai, F. Meirer, E. T. C. Vogt, P. C. A. Bruijnincx, H. C. Gerritsen, B. M. Weckhuysen, *Angew. Chemie - Int. Ed.* **2018**, *57*, 257–261.
[17] G. T. Whiting, N. Nikolopoulos, I. Nikolopoulos, A. D. Chowdhury, B. M. Weckhuysen, *Nat. Chem.* **2019**, *11*, 23–31.
[18] M. Gao, H. Li, W. Liu, Z. Xu, S. Peng, M. Yang, M. Ye, Z. Liu, *Nat. Commun.* **2020**, *11*, DOI 10.1038/s41467-020-17355-6.
[19] E. Heracleous, E. Pachatouridou, A. M. Hernández-Giménez, H. Hernando, T. Fakin, A. L. Paioni, M. Baldus, D. P. Serrano, P. C. A. Bruijnincx, B. M. Weckhuysen, A. A. Lappas, *J. Catal.* **2019**, *380*, 108–122.
[20] L. Karwacki, E. Stavitski, M. H. F. Kox, J. Kornatowski, B. Weckhuysen, *Angew. Chemie - Int. Ed.* **2007**, *46*, 7228–7231.
[21] L. Karwacki, B. M. Weckhuysen, *Phys. Chem. Chem. Phys.* **2011**, *13*, 3681–3685.
[22] N. Omori, A. G. Greenaway, M. Sarwar, P. Collier, G. Valentini, A. M. Beale, A. Candeo, *J. Phys. Chem. C* **2020**, *124*, 531–543.
[23] J. R. Lakowicz, H. Szmacinski, K. Nowaczyk, K. W. Berndt, M. Johnson, *Anal. Biochem.* **1992**, *202*, 316–330.
[24] M. Busby, C. Blum, M. Tibben, S. Fibikar, G. Calzaferri, V. Subramaniam, L. De Cola, *J. Am. Chem. Soc.* **2008**, *130*, 10970–10976.
[25] M. M. Yatskou, M. Meyer, S. Huber, M. Pfenniger, G. Calzaferri, *ChemPhysChem* **2003**, *4*, 567–587.
[26] W. Schrimpf, J. Jiang, Z. Ji, P. Hirschle, D. C. Lamb, O. M. Yaghi, S. Wuttke, *Nat. Commun.* **2018**, *9*, DOI 10.1038/s41467-018-04050-w.
[27] M. A. Digman, V. R. Caiolfa, M. Zamai, E. Gratton, *Biophys. J.* **2008**, *94*, 14–16.
[28] D. Comelli, G. Valentini, A. Nevin, A. Farina, L. Toniolo, R. Cubeddu, *Rev. Sci. Instrum.* **2008**, *79*, 86112.
[29] P. Colarusso, L. H. Kidder, I. W. Levin, J. C. Fraser, J. F. Arens, E. N. Lewis, *Appl. Spectrosc.* **1998**, *52*, 106A-120A.
[30] Y. Hiraoka, T. Shimi, T. Haraguchi, *Cell Struct. Funct.* **2002**, *27*, 367–374.
[31] A. M. Rivera-Figueroa, K. A. Ramazan, B. J. Finlayson-Pitts, *J. Chem. Educ.* **2004**, *81*, 242–245.
[32] A. D. Wheatley, S. Sadhra, *J. Liq. Chromatogr. Relat. Technol.* **1998**, *21*, 2509–2521.
[33] Y. Mu, N. Wang, Z. Sun, J. Wang, J. Li, J. Yu, *Chem. Sci.* **2016**, *7*, 3564–3568.
[34] W. Zhao, B. Basnet, I. J. Kim, *J. Adv. Ceram.* **2012**, *1*, 179–193.
[35] H. G. Baldovi, S. Valencia, M. Alvaro, A. M. Asiri, H. Garcia, *Nanoscale* **2015**, *7*, 1744–1752.
[36] M. C. Ortega-Liebana, N. X. Chung, R. Limpens, L. Gomez, J. L. Hueso, J. Santamaria, T. Gregorkiewicz, *Carbon N. Y.* **2017**, *117*, 437–446.
[37] E. Bourgeat-Lami, F. Di Renzo, F. Fajula, P. H. Mutin, T. Des Courieres, *J. Phys. Chem.* **1992**, *96*, 3807–3811.
[38] S. Hashimoto, *J. Photochem. Photobiol. C Photochem. Rev.* **2003**, *4*, 19–49.
[39] H. L. Casal, J. C. Scaiano, *Can. J. Chem.* **1984**, *62*, 628–629.
[40] J. Goetze, F. Meirer, I. Yarulina, J. Gascon, F. Kapteijn, J. Ruiz-Martínez, B. M. Weckhuysen, *ACS Catal.* **2017**, *7*, 4033–4046.
[41] P. K. Dutta, D. C. Shieh, M. Puri, *J. Phys. Chem.* **1987**, *91*, 2332–2336.
[42] Y. Yu, G. Xiong, C. Li, F. S. Xiao, *Microporous Mesoporous Mater.* **2001**, *46*, 23–34.
[43] H. Shinohara, Y. Yamakita, K. Ohno, *J. Mol. Struct.* **1998**, *442*, 221–234.
[44] E. Cloutis, P. Szymanski, D. Applin, D. Goltz, *Icarus* **2016**, *274*, 211–230.
[45] J. Dědeček, L. Čapek, P. Sazama, Z. Sobalík, B. Wichterlová, *Appl. Catal. A Gen.* **2011**, *391*, 244–253.

Entry for the Table of Contents